

# *Ab initio* modeling of nonequilibrium dynamics in superconducting detectors and qubits

Alejandro Simon,\* Reed Foster, James Shi, Emma Batson, Francesca Incalza, Matteo Castellani, Owen Medeiros, and Karl K. Berggren  
*Department of Electrical Engineering and Computer Science, Massachusetts Institute of Technology  
50 Vassar Street, Cambridge, MA, USA, 02139-4307*

Mihir Sahoo and Christoph Heil  
*Institute of Theoretical and Computational Physics,  
Graz University of Technology  
Petersgasse 16, 8010 Graz, Austria  
(Dated: May 20, 2025)*

Nonequilibrium quasiparticle and phonon dynamics are central to the operation of superconducting devices. Superconducting detectors, such as superconducting nanowire single-photon detectors, transition-edge sensors, or microwave kinetic inductance detectors, perform best when a large quasiparticle population is generated in response to small perturbations. Conversely, for superconducting qubits and topologically protected Majorana fermions, even relatively small quasiparticle densities can lead to significant performance degradation. Hence, ideal materials for these devices would be less susceptible to quasiparticle poisoning. However, existing models of these devices often rely on approximations and phenomenology. Therefore, they lack a rigorous description of the underlying quasiparticle and phonon dynamics that are responsible for device performance. In this article, we combine kinetic equations with density functional theory to model the non-equilibrium quasiparticle and phonon dynamics of a thin superconducting film *ab initio*. To demonstrate the universality of our model, we illustrate two independent example applications: (1) we develop a theoretical model describing the detection of single photons in superconducting nanowires, and (2) we calculate the energy-relaxation rate of a transmon qubit due to the presence of excess quasiparticles. Our examples demonstrate from first principles that niobium nitride is well-suited to be used for single-photon detection and that tantalum transmon qubits possess reduced sensitivity to quasiparticle poisoning relative to other materials, which is likely in part responsible for their longer coherence times. In contrast to previous models of superconducting devices, our *ab initio* approach makes predictions of device performance without experimental input and thus can be used to accelerate progress in device development. Moreover, by considering the full-bandwidth electron-phonon coupling, our approach can incorporate strong-coupling effects. Our methods effectively integrate *ab initio* materials modeling with nonequilibrium theory of superconductivity to perform practical modeling of superconducting devices, providing a comprehensive approach that connects fundamental theory with device-level applications.

## I. INTRODUCTION

The success of the Migdal-Eliashberg theory has illustrated the importance of considering the full-bandwidth electron-phonon coupling spectrum to describe conventional superconductivity [1–3]. However, the full-bandwidth electron-phonon coupling not only provides insights into equilibrium superconductivity but also lays the foundation for understanding nonequilibrium phenomena, where the electron-phonon coupling determines the evolution of the quasiparticle and phonon distributions. These distributions, in turn, influence the modification of the transport properties of a material when subjected to external perturbations, such as radiation absorption or heating [4–7]. However, obtaining the full-bandwidth electron-phonon coupling spectrum for arbitrary materials has historically been difficult. Thus, studies of the nonequilibrium dynamics of superconductors

typically rely on approximating the phonon system with a Debye model [7–10]. This approximation, which assumes a linear dispersion for the phonons, is generally inadequate for capturing realistic electron-phonon coupling. Therefore, the Debye model can only provide qualitative predictions and cannot be used to describe general nonequilibrium superconductivity.

This limitation of the Debye model is a critical issue for device modeling, as nonequilibrium dynamics are central to the operation of many superconducting devices. To overcome this limitation, we developed an *ab initio* model to quantitatively predict the microscopic response of a thin, narrow superconducting film to external perturbation. To do so, we employ recent advances in *ab initio* materials modeling within the framework of Density Functional Perturbation Theory (DFPT) [11, 12]. The resulting model is of particular interest for the development and study of superconducting detectors [13, 14], microwave resonators [15], and quasiparticle poisoning of qubits [16, 17].

In the following, we formulate the theory behind this

\* Corresponding author: alejansi@mit.edu

model and apply it in two independent examples: (1) to describe a film irradiated by optical photons and (2) to describe the energy-relaxation rate of a transmon qubit. To connect our first example with experiment, we use our model to predict the wavelength sensitivity of a superconducting nanowire single-photon detector (SNSPD) by determining the detection current  $I_{\text{det}}$ , defined as the current at which the internal detection efficiency of an SNSPD saturates for a given photon wavelength and device temperature, and compare our results to experimental data. For our second example, we study the energy-relaxation rate of the transmon when impacted by ionizing radiation. For comparison with experimental results, we focus on niobium nitride (NbN) when modeling optical irradiation and aluminum (Al), niobium (Nb), titanium nitride (TiN), lead (Pb), and tantalum (Ta) when modeling transmon energy-relaxation rates; however, the methods outlined here are suitable to describe any conventional isotropic superconductor and can be generalized to incorporate anisotropy [4]. We also emphasize that as an *ab initio* theory, the predictions of this model are based on first-principles calculations of the material's properties and can be made with no experimental input.

## II. MODEL FORMULATION

When a superconductor is perturbed, excess quasiparticles and/or phonons are generated. The resulting nonequilibrium dynamics of the relaxation process can be described by a set of kinetic equations for the quasiparticle  $f(E)$  and phonon  $n(\Omega)$  distribution functions, which for an isotropic material and neglecting diffusion are

$$\begin{aligned} \frac{df(E)}{dt} = & -\frac{2\pi}{\hbar} \int_0^\infty d\Omega \alpha^2 F(\Omega) \rho(E + \Omega) K_{\text{ph}-e}(E, \Omega) \\ & -\frac{2\pi}{\hbar} \int_0^{E-|\Delta|} d\Omega \alpha^2 F(\Omega) \rho(E - \Omega) K_{e-\text{ph}}(E, \Omega) \\ & -\frac{2\pi}{\hbar} \int_{E+|\Delta|}^\infty d\Omega \alpha^2 F(\Omega) \rho(\Omega - E) K_{\text{R}}(E, \Omega) \end{aligned} \quad (1a)$$

and

$$\begin{aligned} \frac{dn(\Omega)}{dt} = & -\frac{8\pi}{\hbar} \frac{N(0)}{N} \int_{|\Delta|}^\infty dE \int_{|\Delta|}^\infty dE' \alpha^2(\Omega) \rho(E) \rho(E') \\ & \times \left[ K_{\text{S}}(E, E', \Omega) \delta(E + \Omega - E') \right. \\ & \left. + K_{\text{B}}(E, E', \Omega) \delta(E + E' - \Omega) \right] - \frac{n(\Omega) - n^{\text{eq}}(\Omega)}{\tau_{\text{esc}}}, \end{aligned} \quad (1b)$$

where the integral kernels  $K_i$  are functions of  $f(E)$  and  $n(\Omega)$  and are defined in the Appendix.  $K_{\text{ph}-e}(E, \Omega)$  ( $K_{e-\text{ph}}(E, \Omega)$ ) describes quasiparticle scattering due to the absorption (emission) of a phonon, while  $K_{\text{R}}(E, \Omega)$  represents the quasiparticle recombination

process.  $K_{\text{S}}(E, E', \Omega)$  captures the phonon scattering process, and  $K_{\text{B}}(E, E', \Omega)$  describes the phonon pair-breaking process. Here,  $N$  is the number of ions per unit volume, and  $\rho(E)$  is the normalized quasiparticle density of states [7]. These equations are valid in cases where the quasiparticle approximation holds, i.e., when the quasiparticle lifetimes are sufficiently long, corresponding to well-defined states. This is true for the excitation energies of interest in this paper, which are below the characteristic phonon frequency  $\omega_{\text{D}}$  even in the case of optical irradiation. In Eqs. (1a) and (1b), it is also assumed that renormalization effects are small and that the imaginary component of the order parameter  $\Delta$  is negligible. For small excitation frequencies relative to  $\omega_{\text{D}}$ , we may also neglect the frequency dependence of  $\Delta$ . For a film in the dirty limit, characterized by  $l_e \ll \xi_c$ ,  $\rho(E)$  can be calculated for a finite bias current  $I_{\text{B}}$  by solving the Usadel equation as detailed in the Appendix. Solutions to the Usadel equation for  $\rho(E)$  at various bias currents are displayed in Fig. 2a. With the above simplifications, the superconducting order parameter  $\Delta$  satisfies

$$|\Delta| = \lambda \int_{|\Delta|}^\infty dE R(E, \Delta) [1 - 2f(E)], \quad (2)$$

where  $\lambda = 2 \int_0^\infty d\Omega \alpha^2 F(\Omega) / \Omega$  is the electron-phonon coupling parameter and  $R(E, \Delta)$  is a spectral function defined in the Appendix [7, 13]. The final term of Eq. (1b) models phonon exchange with the substrate, where  $n^{\text{eq}}(\Omega)$  is the usual Bose-Einstein distribution and  $\tau_{\text{esc}}$  is the characteristic time for phonon escape to the substrate. To simplify calculations, we ignore the energy and angular dependence of  $\tau_{\text{esc}}$ .

In Eqs. (1a) and (1b), the quasiparticle and phonon interaction probabilities are determined by the Eliashberg spectral function  $\alpha^2 F(\Omega)$  and the phonon density of states  $F(\Omega)$ . In general,  $\alpha^2 F(\Omega)$  and  $F(\Omega)$  can be obtained experimentally through electron-tunneling and inelastic neutron-scattering measurements, respectively. However, with DFPT, we can computationally obtain these quantities *ab initio* for a wide range of conventional superconductors, including superconducting alloys and anisotropic materials [11, 18], circumventing the need for experimental data. As we show in Fig. 1e, in our model, we combine DFPT calculations with Eqs. (1a) and (1b) to model the nonequilibrium quasiparticle and phonon dynamics. In Fig. 2b, we display the calculated acoustic phonon dispersion for the  $\delta$ -NbN phase within the harmonic approximation and experimental data obtained via neutron scattering for  $\delta$ -NbN<sub>0.93</sub> [19]. Notably, the agreement is strong for the acoustic branches, which exhibit the strongest electron-phonon coupling, underscoring the validity of our theoretical approach. Details of the DFPT calculations are contained in the Appendix. We also include DFPT-calculated  $\alpha^2 F(\Omega)$  and  $F(\Omega)$  for Al, Nb, TiN, Pb, and Ta in Fig. 2c-g.

In Fig. 2b,  $\alpha^2 F(\Omega)$  and  $F(\Omega)$  for NbN are displayed alongside the Debye model, where a quadratic frequency dependence is assumed with  $\alpha^2 F(\Omega) = \lambda \Omega^2 / \Omega_{\text{D}}^2$  and

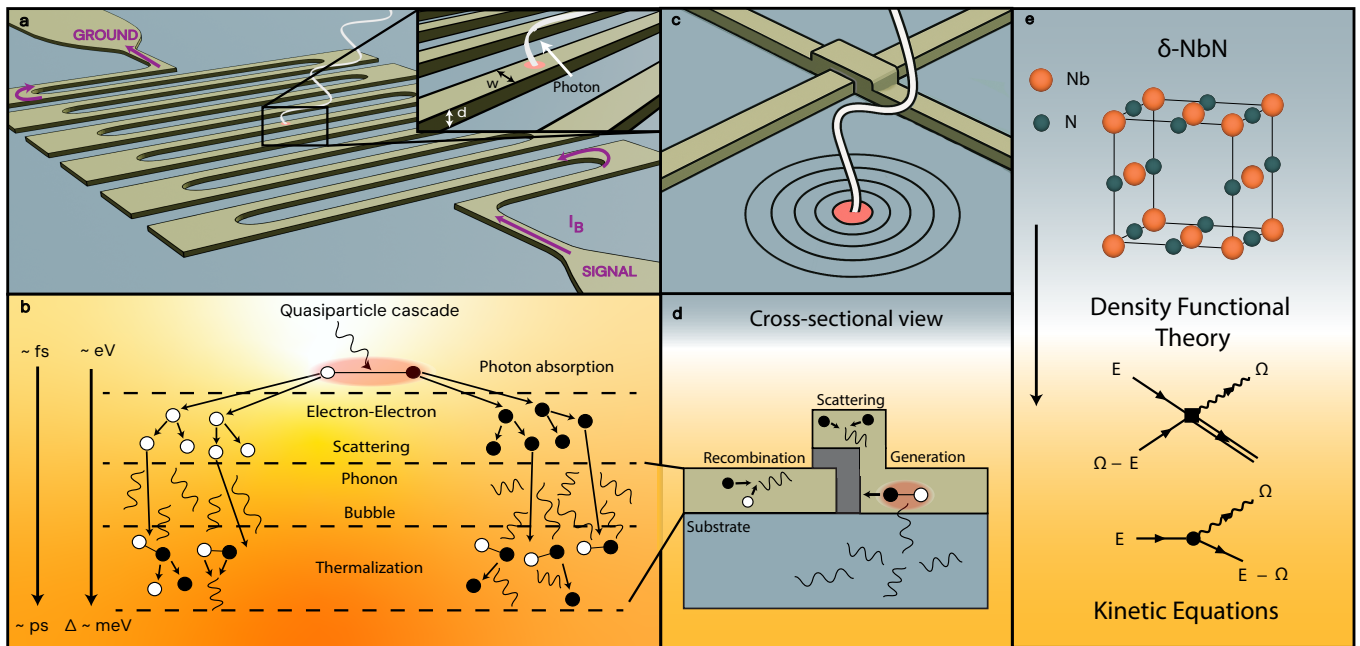


FIG. 1. High-level overview of the modeling of nonequilibrium devices. (a) Typical SNSPD geometry consisting of a thin ( $d \sim \xi_c$ ) narrow ( $w \ll \Lambda$ ) superconducting wire that is patterned in a meander to increase the active area of the detector. The device is single-photon sensitive when a sufficiently large bias current  $I_B$  is applied. (b) Microscopic picture of SNSPD detection. A photon is absorbed, generating an excited quasiparticle consisting of an electron-hole pair. This excitation triggers an energy-relaxation cascade and the generation of a phonon bubble. The resulting quasiparticles and phonons scatter and break pairs, locally suppressing the superconductivity and weakening the barrier for quantum and thermal fluctuations that may fully destroy the superconductivity across the strip. Due to the bias current, this normal strip produces a nonzero voltage across the terminals of the device, which is read out as a detection event. (c) A cartoon depiction of the Manhattan-style Josephson junction commonly used in transmon qubit fabrication. A cosmic ray interacts with the substrate, generating a large population of phonons that perturb the superconductivity in the Josephson junction. (d) Cross-sectional view of the process in (c). The quasiparticle recombination, scattering, and generation processes are displayed inside the superconducting layer of the Josephson junction. These processes are identical to those in the phonon bubble and thermalization steps shown in (b). (e) *Ab initio* approach to modeling nonequilibrium dynamics in superconductors. Beginning with the crystal structure, we obtain the electron-phonon coupling with density functional theory, which allows us to obtain the interaction probabilities for the quasiparticle and phonon systems. The evolution of the quasiparticle and phonon distributions is then modeled using a set of kinetic equations.

$F(\Omega) = 9\Omega^2/\Omega_D^3$  for  $\Omega < \Omega_D$  and zero otherwise, where  $\Omega_D$  is the Debye frequency [7, 10]. This comparison clearly shows that the structure of  $\alpha^2 F(\Omega)$  and  $F(\Omega)$  is neglected in the Debye approximation. Given the importance of these quantities in determining the interaction probabilities, one must consider their precise forms to make quantitative predictions of the nonequilibrium quasiparticle and phonon dynamics.

### III. OPTICAL IRRADIATION

Due to their exceptional performance characteristics, superconducting single-photon detectors, such as the SNSPD, transition-edge sensor, and microwave kinetic inductance detector, have quickly become ubiquitous in sensing, communication, and computing applications. In particular, SNSPDs have earned widespread recognition for demonstrations of near-unity internal single-

photon detection efficiency [20–22], single-photon sensitivity from X-rays to mid-infrared wavelengths [23, 24], ultra-low dark-count rates [25, 26], and sub-3 ps timing jitter [27]. However, applications such as dark matter search, biomedical imaging, and space communication can benefit considerably from improvements in the operating temperature and wavelength sensitivity of these detectors. Consequently, there is a large effort directed at engineering and exploring new materials for enhanced SNSPD performance [22, 24, 27–34].

To direct this effort, a precise understanding of the mechanism underpinning photon detection in SNSPDs is required [13, 14, 35–44]. To this end, several phenomenological models of photon detection in superconducting nanowires have been proposed; however, these models are generally unsatisfactory for describing arbitrary SNSPD geometries and materials. Prior work has demonstrated the crucial role of quasiparticle and phonon interactions in the initial stages of photon detec-

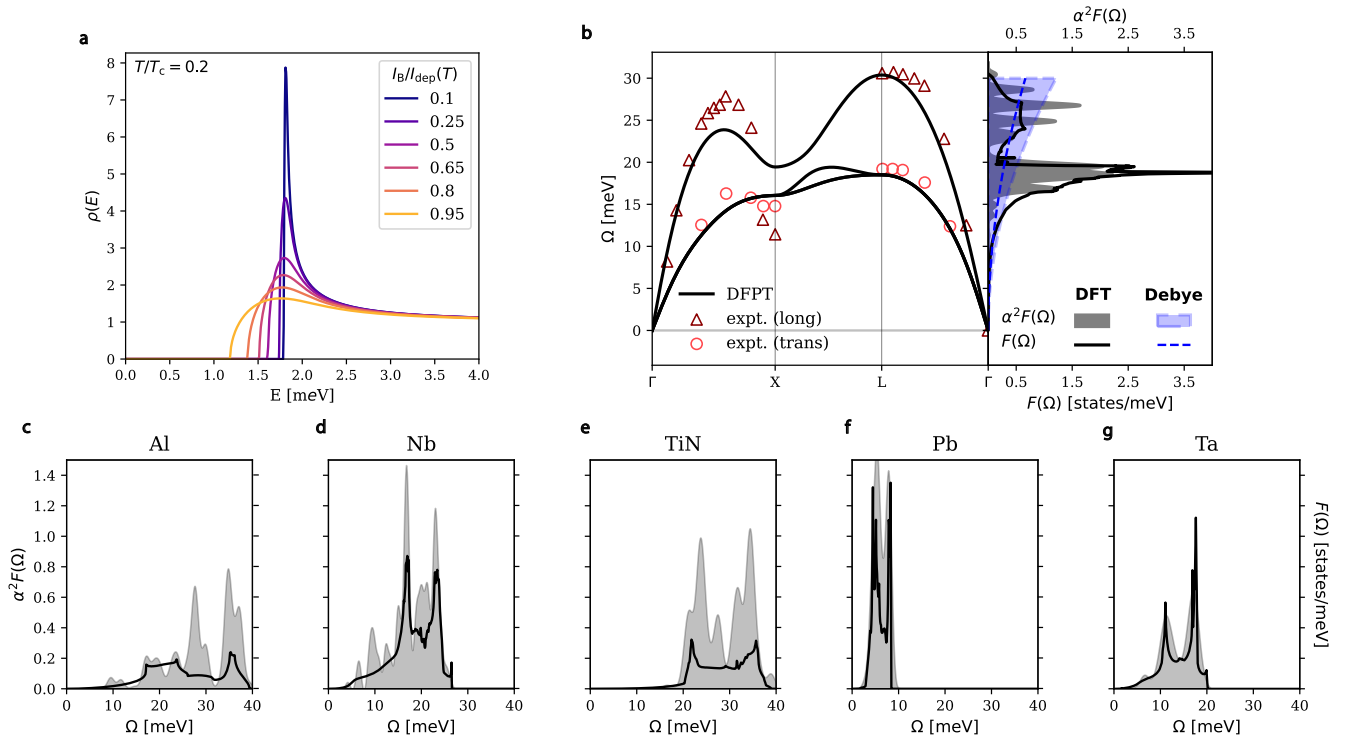


FIG. 2. (a) Normalized quasiparticle density of states  $\rho(E)$  for  $\delta$ -NbN with  $T_c = 10$  K and different ratios of the bias current normalized to the depairing current  $I_B/I_{\text{dep}}(T)$ . (b) Acoustic phonon modes for  $\delta$ -NbN calculated using density functional perturbation theory compared to experimental data for the longitudinal and transverse modes [19]. The corresponding Eliashberg spectral function  $\alpha^2 F(\Omega)$  (solid grey) and phonon density of states  $F(\Omega)$  (black) are displayed on the right compared to the Debye approximation (dashed and solid blue). Density functional perturbation theory calculated results are also displayed for (c) aluminum, (d) niobium, (e) titanium nitride, (f) lead, (g) tantalum. Spin-orbit coupling effects were included for lead and tantalum.

tion [13, 14, 40–42, 45]. Only a limited number of studies have attempted to model these interactions directly [13, 14, 40]; however, these studies have relied on the Debye approximation, consequently neglecting the effect of realistic electron-phonon coupling.

In this work, we address this limitation with the *ab initio* model. We consider a typical SNSPD geometry, consisting of a thin, narrow superconducting wire that has absorbed a single optical photon while carrying a nonzero bias current  $I_B$ . As depicted in Fig. 1a, such a film is characterized by a thickness on the order of the superconducting coherence length  $d \sim \xi_c = \sqrt{\hbar D/|\Delta|}$  and width much smaller than the Pearl length  $w \ll \Lambda = 2\lambda_L^2/d$ , where  $\lambda_L$  is the London penetration depth ( $\lambda_L = \sqrt{\hbar \rho_N/\mu_0 \pi |\Delta|}$ ),  $\rho_N$  is the normal state resistivity ( $\rho_N = 1/2e^2 D N(0)$ ),  $e$  is the electron charge,  $N(0)$  is the single-spin electron density of states at the Fermi energy  $E_F$ ,  $\mu_0$  is the permeability of free-space,  $\hbar$  is the reduced Planck constant,  $D$  is the electronic diffusion coefficient ( $D = v_F l_e/3$ ),  $v_F$  is the Fermi velocity,  $l_e$  is the electron mean-free path, and  $|\Delta|$  is the magnitude of the superconducting order parameter. In general,  $|\Delta|$  is a function of temperature  $T$ ,  $I_B$ , and position  $\mathbf{r}$ .

When a photon is absorbed in the superconducting

film, a single quasiparticle is excited with an energy  $E_\lambda \gg |\Delta|$ . The lifetime of a quasiparticle of energy  $\sim E_\lambda$  is extremely short relative to the timescale of variations of the superconducting order parameter  $\tau_\Delta = \hbar/|\Delta|$  [46, 47]. Thus, the subsequent interactions are practically instantaneous from the perspective of  $\Delta$ . Initially, quasiparticle relaxation occurs primarily through electron-electron scattering and the emission of secondary electrons. These electrons quickly reach energies on the order of  $\Omega_D = \hbar\omega_D$ , where relaxation via acoustic-phonon emission dominates [7, 47]. These emitted phonons possess short mean-free paths and contribute to pair-breaking. Hence, the initial distribution for Eqs. (1a) and (1b) is well approximated by a phonon-bubble initial condition [13], which is derived in the Appendix. These dynamics are illustrated in Fig. 1b.

In Fig. 3a and Fig. 3b, numerical solutions to Eqs. (1a) and (1b) for two different electronic diffusion coefficients  $D$  are displayed. In these calculations, material parameters consistent with NbN, and SNSPD geometries were used and can be found in the Appendix.  $D = 1.5 \text{ cm}^2/\text{s}$  is typical of epitaxial NbN [48], while  $D = 0.5 \text{ cm}^2/\text{s}$  is typical of polycrystalline NbN [13]. For smaller  $D$ , corresponding to greater disorder,  $\alpha^2 F(\Omega)$  is

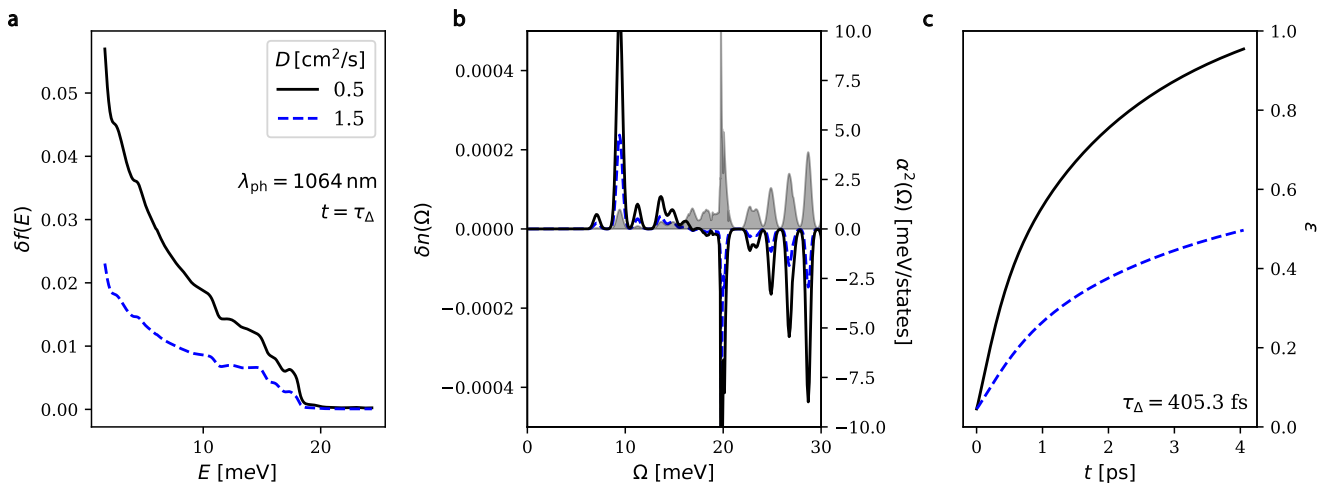


FIG. 3. Solutions to the kinetic equations for  $\delta f(E)$ ,  $\delta n(\Omega)$ , and  $\epsilon(t)$  for NbN. (a) Nonequilibrium excess quasiparticle  $\delta f(E)$  and (b) excess phonon  $\delta n(\Omega)$  distribution generated by the absorption of a photon with wavelength  $\lambda_{\text{ph}} = 1064$  nm at  $t = \tau_{\Delta}$  for NbN with electronic diffusion coefficients of  $D = 0.5$  cm<sup>2</sup>/s (solid black lines) and  $D = 1.5$  cm<sup>2</sup>/s (dashed blue lines). In (b),  $\alpha^2(\Omega)$  for NbN is displayed on the right axis. (c) Quasiparticle-induced suppression parameter  $\epsilon(t)$ . A value of  $\epsilon = 0$  implies no suppression of  $\Delta$ .

smeared; however, we do not expect this effect to have a significant impact on our results, and thus, we neglect it. In our solutions, we assume that the photon's energy is initially distributed uniformly in a cylindrical volume of  $V_{\text{init}} = \pi \xi_c^2 d$  and  $|\Delta(I_B, T)|$  is constant for the timescales of interest ( $t \sim \tau_{\Delta}$ ). Further details regarding the numerical methods and validation are discussed in the Appendix.

By inserting  $\delta f(E)$  into Eq. (2) we calculate the quasiparticle-induced suppression parameter

$$\epsilon(t) = 2 \int_{|\Delta|}^{\infty} dE \frac{R(E, \Delta)}{|\Delta|} \delta f(E), \quad (3)$$

which characterizes the suppression of  $|\Delta|$  and is displayed in Fig. 3c. Fig. 3c illustrates that in dirtier materials with a smaller  $D$ , a larger nonequilibrium quasiparticle population is generated within  $V_{\text{init}}$ , resulting in a more significant suppression of  $|\Delta|$  in the initial stages following photon absorption. These results are consistent with the argument that a larger  $D$  leads to more stringent requirements on the detector's geometry to maintain photon sensitivity, e.g., reducing the film thickness and/or wire width [49].

We define the thermalization time of the quasiparticle and phonon system  $\tau_{\text{th}}$  by fitting the numerical solution for  $\epsilon(t)$  to an exponential  $\epsilon(t) = \epsilon_{t \rightarrow \infty} (1 - e^{-t/\tau_{\text{th}}})$ . For NbN at  $T/T_c = 0.2$  with an electronic diffusion coefficient of  $D = 0.5$  cm<sup>2</sup>/s we find  $\tau_{\text{th}} = 1.4$  ps and for  $D = 1.5$  cm<sup>2</sup>/s we find  $\tau_{\text{th}} = 1.8$  ps for a photon wavelength of  $\lambda_{\text{ph}} = 1064$  nm. That  $\tau_{\text{th}} > \tau_{\Delta} = 405.3$  fs is consistent with results obtained with the Debye model [13]; however, with the Debye model it is found that, for  $D = 0.5$  cm<sup>2</sup>/s,  $\tau_{\text{th}} \approx 1.5\tau_{\Delta}$ , whereas with the full-bandwidth electron-phonon coupling, we find  $\tau_{\text{th}} \approx 4\tau_{\Delta}$ .

The larger value of  $\tau_{\text{th}}$  obtained with the full-bandwidth electron-phonon coupling is in better agreement with experimental data [47].

The microscopic treatment above is only suitable to account for the local suppression of superconductivity within  $V_{\text{init}}$  for  $t \sim \tau_{\Delta}$ . To determine if the suppression is sufficient to create a normal strip across the film, we must examine the two-dimensional dynamics of  $\Delta$ , including quantum fluctuations of the phase. These fluctuations are critical to consider, as experimental and theoretical evidence suggests that detection in SNSPDs is assisted by vortex motion or phase-slippage [43, 52]. In this picture, the suppression of superconductivity induced by the photon lowers the barrier for a  $2\pi$ -phase-slip of  $\Delta$ . Several processes can lead to phase-slip events in nanowires, including (1) the passage of a single vortex across the wire; (2) a quantum or thermally activated phase-slip; or (3) a vortex/anti-vortex pair that unbinds due to the Magnus force from  $I_B$ . We refer to these processes collectively as phase-slip events. Once a phase-slip event occurs, Joule heating due to the nonzero  $I_B$  can lead to thermal runaway, destroying superconductivity across the strip and resulting in a voltage spike corresponding to a detection event. We describe our calculation of the phase-slip rate using the time-dependent Ginzburg-Landau (TDGL) equation in the Appendix.

In Fig. 4a-c, we show the resulting dependence of  $I_{\text{det}}$  on  $\lambda_{\text{ph}}$ . We note in comparing our model against  $I_{\text{det}}$ , which corresponds to the onset of the plateau (90%) in the photon count rate (PCR) curve, we have implicitly assumed that spatial inhomogeneities and thermal fluctuations dominate the shape of the PCR curve in NbN. If Fano fluctuations were the dominant fluctuations, we would expect our model instead to provide predictions closer to the inflection point of the PCR curve [53], and

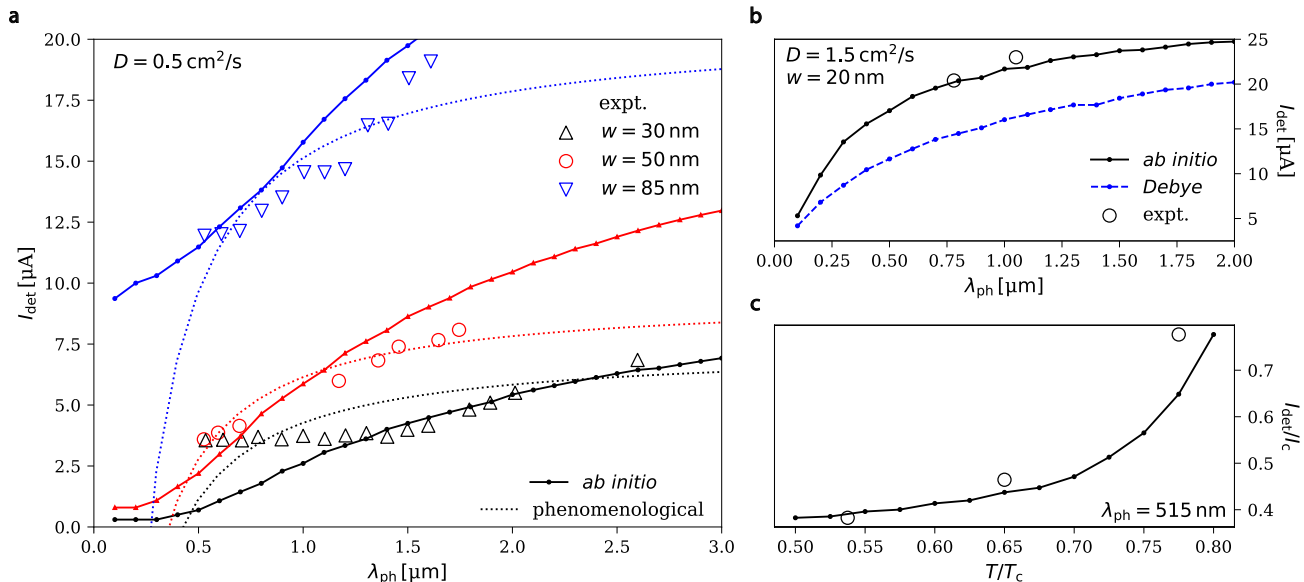


FIG. 4. A comparison of the *ab initio* model (solid lines) against the phenomenological diffusive hotspot model [35, 45] (dotted lines), Debye model (dashed lines), and experimental data (large open markers) [49–51]. (a) Determination of the detection current  $I_{\text{det}}$  for a given photon wavelength  $\lambda_{\text{ph}}$  and wire widths of  $w = 30 \text{ nm}$ ,  $50 \text{ nm}$ , and  $85 \text{ nm}$  with  $D = 0.5 \text{ cm}^2/\text{s}$  compared to the experimental data of Ref. [50]. A value of  $\eta = 0.2$  for the diffusive hotspot model gives the best fit (See Ref. [45] for a definition of  $\eta$ ). (b)  $I_{\text{det}}$  as a function of  $\lambda_{\text{ph}}$  for  $w = 20 \text{ nm}$  and parameters consistent with the material used in the experimental data of Ref. [49]. Results using both the full-bandwidth electron-phonon coupling (*ab initio*) and Debye model are displayed. (c) *Ab initio* predictions of the normalized detection current  $I_{\text{det}}/I_c$  as a function of the reduced temperature  $T/T_c$  for  $\lambda_{\text{ph}} = 515 \text{ nm}$  compared to experimental data for the temperature-dependence of NbTiN from Ref. [51]. Since the data in this figure is not for NbN, only qualitative agreement of the temperature dependence is expected. Calculations from the *ab initio* model are in arbitrary units.

the experimental data in Fig. 4a-c should be shifted downward correspondingly. We compare our calculations with the phenomenological diffusive normal-core model [35, 45], Debye model, and experimental data from Ref. [49, 50]. We also check for qualitative agreement of the temperature dependence of  $I_{\text{det}}$  with the experimental data for NbTiN of Ref. [51]. In our calculations, we assumed  $D = 0.5 \text{ cm}^2/\text{s}$  for the polycrystalline detectors in Ref. [50] and  $D = 1.5 \text{ cm}^2/\text{s}$  for the epitaxial detector of Ref. [49]. We observe that the qualitative behavior of the *ab initio* model is similar to the experimental data, and there is reasonable quantitative agreement. The *ab initio* model also improves over the predictions of the diffusive normal-core and Debye models. We emphasize that our model achieves this improved agreement without free parameters, which affirms the merit of our approach. We therefore propose that the methods presented here can be used to design the next generation of SNSPDs by enabling the exploration of new materials and geometries that extend device metrics to new regimes.

As discussed in the Appendix, our TDGL formulation can be further improved and generalized to improve quantitative accuracy, and spatial inhomogeneity and thermal and Fano fluctuations can be incorporated to allow for the determination of the internal detection efficiency below  $I_{\text{det}}$ , timing jitter, and the prediction

of dark count rates [54–56]. Optical absorption efficiency can also be calculated [57–59] and integrated to provide a complete end-to-end model from the crystal structure of a material to photon absorption and the resulting voltage spike and macroscopic circuit dynamics.

#### IV. QUASIPARTICLE-INDUCED DECOHERENCE IN TRANSMON QUBITS

The transmon qubit is currently a leading platform in the race to develop a practical quantum computer [60]. However, since quantum computation is inherently error-prone, useful fault-tolerant quantum computation (FTQC) requires the implementation of error-correcting schemes. These error-correcting algorithms require high-fidelity physical qubits with long coherence times  $T_1$ . Through careful engineering of the design and material platform, transmon qubits have achieved coherence times on the order of hundreds of microseconds. However, this remains below the millisecond-scale coherence times typically desired for practical fault-tolerant quantum computing (FTQC). Further improvements necessitate an improved understanding of the fundamental sources of decoherence and their effects on qubit performance to motivate further engineering.

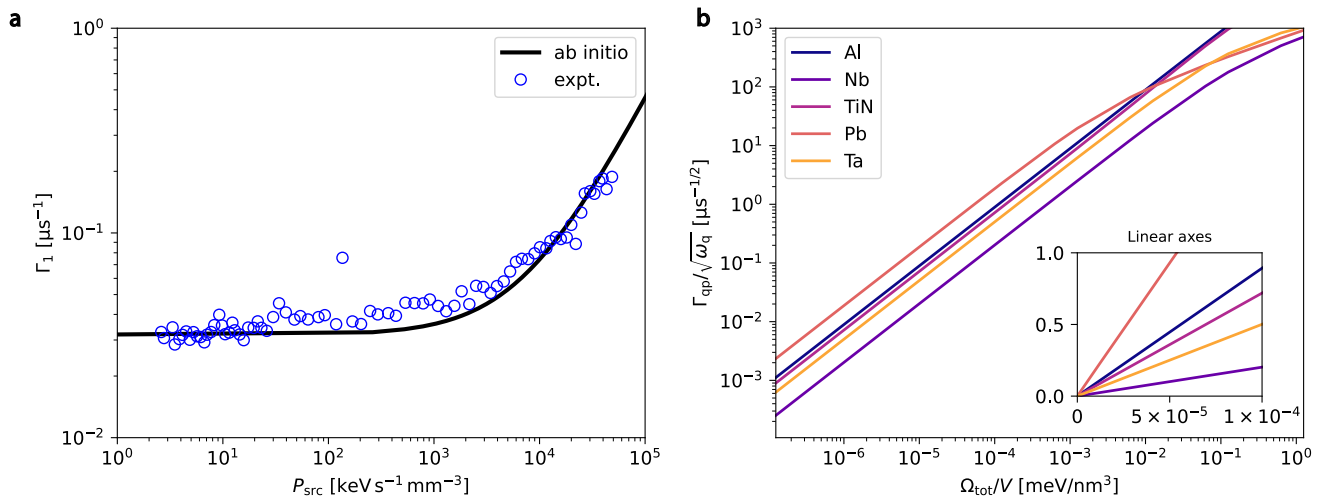


FIG. 5. The energy-relaxation rate  $\Gamma_1 = 1/T_1$  of a transmon qubit. (a)  $\Gamma_1$  as a function of the radiation power density of a  $\text{Cu}^{64}$  source as described in Ref. [61]. The *ab initio* prediction is depicted with the experimental data. (b) Predictions from the *ab initio* model of the dependence of  $\Gamma_{\text{qp}}$  on absorbed phonon energy density  $\Omega_{\text{tot}}/V$ . Aluminum is found to be the most susceptible to quasiparticle poisoning, whereas niobium is the least.

Experimental data suggest that nonequilibrium quasiparticles play a role in correlated noise and decreasing  $T_1$  in superconducting qubits [61, 62]. Indeed, measurements of the quasiparticle densities in superconducting qubits have suggested that populations of nonequilibrium quasiparticles do not follow a thermal distribution near millikelvin temperatures ( $\lesssim 150$  mK in Al) due to an excess of quasiparticles [62]. These nonequilibrium populations have been attributed to the sensitivity of superconducting qubits to environmental radiation, including cosmic rays and the presence of naturally embedded radioactive isotopes in the environment [61]. This radiation is either absorbed in the substrate, and the energy is transferred to the qubit via phonons originating in the substrate, or it can be directly absorbed by the Cooper pairs in the qubit. This process is depicted in Fig. 1c-d.

The impact of nonequilibrium quasiparticles on  $T_1$  is described by

$$\Gamma_1 = \frac{1}{T_1} = \Gamma_{\text{qp}} + \Gamma_{\text{other}}, \quad (4)$$

where  $\Gamma_{\text{qp}}$  is the energy-relaxation rate due to nonequilibrium quasiparticles and  $\Gamma_{\text{other}}$  encompasses all other loss mechanisms, including dielectric and two-level system losses. For a transmon,  $\Gamma_{\text{qp}}$  is given by

$$\Gamma_{\text{qp}} = \sqrt{\frac{2\omega_q|\Delta|}{\pi^2\hbar}} x_{\text{qp}}, \quad (5)$$

where  $\omega_q$  is the qubit frequency and  $x_{\text{qp}} = n/n_{\text{cp}}$  is the density of quasiparticles  $n$  normalized to the density of Cooper pairs in the material  $n_{\text{cp}}$  [61, 63]. As expected, Eqs. (4) and (5) suggest that  $\Gamma_1$  can be reduced by decreasing the quasiparticle density  $x_{\text{qp}}$ . To do so requires

engineering the qubit or its substrate to reduce the rate of phonons transferred to the qubit or exploring alternative material platforms that may inherently possess a weaker response to environmental radiation. In both cases, a quantitatively accurate model of the qubit response to perturbation is desirable.

Existing efforts to understand the qubit response to quasiparticle poisoning have relied on the quasiparticle dynamics provided by the Rothwarf-Taylor model [61, 63], which is a phenomenological description of quasiparticle recombination, scattering, and generation<sup>1</sup>. These models lack a rigorous description of these rates and rely on fitting to experimental data, hence limiting their applicability to exploring novel materials or physics. Our model is well-suited to fill this gap since it can predict these rates from more fundamental material properties, enabling the comparison of quasiparticle dynamics across a wide range of materials.

In Fig. 5a, we present calculations of  $\Gamma_1$  for an Al-based transmon using the DFPT calculations shown in Fig. 2c.  $\Gamma_1$  is calculated for different radiation source power densities  $P_{\text{src}}$ , allowing us to compare our model with the experimental data of Ref. [61]. To determine  $\Gamma_1$  from our model, we injected an initial phonon distribution with a modified phonon bubble initial condition as detailed in the Appendix. An energy  $\chi P_{\text{src}}$  was used for the phonon bubble, where  $\chi = 3.5 \times 10^4$  s determines the percentage of energy deposited into the qubit from phonons in the substrate. A rigorous determination of  $\chi$  is possible through a detailed accounting of the phonon

<sup>1</sup> The Rothwarf-Taylor equations can be derived from Eqs. (1a) and (1b) [7].

dynamics in the substrate in a simulation package such as Geant4 [63]. For each energy, we solved Eqs. (1a) and (1b) for the thermalized quasiparticle distribution and extracted the resulting quasiparticle density. Eq. (5) was then used to compute  $\Gamma_{\text{qp}}$  for each  $P_{\text{src}}$ .  $\Gamma_{\text{other}}$  was determined by averaging  $\Gamma_1$  over the 10 lowest  $P_{\text{src}}$  experimental data points. As evidenced by Fig. 5a, we obtained good agreement using our approach.

To compare the susceptibility of different materials to ambient radiation, we calculated  $\Gamma_{\text{qp}}$  for Al, Nb, TiN, Ta, and Pb for different injected phonon energy densities  $\Omega_{\text{tot}}/V$ . The material parameters used in the simulations are listed in the Appendix, and parameters not unique to the materials were kept consistent in the simulations. In Fig. 5b, the results of the calculations for each material are displayed for direct comparison. Al was found to be the most susceptible to quasiparticle poisoning, which is unsurprising because of its relatively small superconducting gap. At  $\Omega_{\text{tot}}/V$ ,  $\Gamma_{\text{qp}}$  exhibits a similar dependence for all materials; however, the rates of quasiparticle generation in different materials diverge at larger  $\Omega_{\text{tot}}/V$ , with Nb, Pb, and Ta increasing at a slower rate than Al and TiN. Interestingly, our *ab initio* model predicts a low susceptibility to quasiparticle poisoning in Ta that is on par with larger gap superconductors like Nb and Pb. This result may in part explain the reduced quasiparticle tunneling rate and longer coherence times observed in Ta transmon qubits [64, 65].

## V. CONCLUSIONS & OUTLOOK

In summary, we have demonstrated a framework for modeling the performance of superconducting devices *ab initio*. To illustrate the effectiveness of our approach, we applied our model to describe the detection mechanism of SNSPDs and quasiparticle poisoning of superconducting qubits. We demonstrate that our model improves signif-

icantly over existing phenomenological models of quasiparticle dynamics while using no free parameters. We emphasize that the methods discussed here can be extended to other superconducting devices and materials. Future work may investigate an even larger assortment of materials and devices to search for materials that perform beyond the current state-of-the-art. Recently, there has been an effort to develop *ab initio* methods for searching for high- $T_c$  superconductors [3]. The methods described here may enable a similar systematic search for materials that optimize the performance of superconducting devices.

## VI. ACKNOWLEDGMENTS

The authors are deeply grateful to Rohit Prasankumar and Mukund Vengalattore for their helpful discussions. The authors are also grateful to Jason Allmaras and Phillip Donald Keathley for their insightful feedback on this manuscript. This work was funded in part by the Defense Sciences Office (DSO) of the Defense Advanced Research Projects Agency (DARPA) (HR0011-24-9-0311). AS and EB acknowledge support from the NSF GRFP, RF acknowledges support from the Alan McWhorter fellowship, OM acknowledges support from the NDSEG fellowship. MS and CH acknowledge support from Intellectual Ventures Property Holdings and usage of computational resources of the dCluster of the Graz University of Technology.

## VII. APPENDIX

### A. Numerical solutions to the kinetic equations

The kernel functions in Eqs. (1a) and (1b) of the main text are given by

$$K_{ph-e}(E, \Omega) = \left(1 - \frac{\Delta^2}{E(E + \Omega)}\right) \left\{ f(E)[1 - f(E + \Omega)]n(\Omega) - f(E + \Omega)[1 - f(E)][n(\Omega) + 1] \right\} \quad (6a)$$

$$K_{e-ph}(E, \Omega) = \left(1 - \frac{\Delta^2}{E(E - \Omega)}\right) \left\{ f(E)[1 - f(E - \Omega)][n(\Omega) + 1] - [1 - f(E)]f(E - \Omega)n(\Omega) \right\} \quad (6b)$$

$$K_R(E, \Omega) = \left(1 + \frac{\Delta^2}{E(\Omega - E)}\right) \left\{ f(E)f(\Omega - E)[n(\Omega) + 1] - [1 - f(E)][1 - f(\Omega - E)]n(\Omega) \right\} \quad (6c)$$

$$K_S(E, E', \Omega) = \left(1 - \frac{\Delta^2}{EE'}\right) \left\{ f(E)[1 - f(E')]n(\Omega) - f(E')[1 - f(E)][n(\Omega) + 1] \right\} \quad (6d)$$

$$K_B(E, E', \Omega) = \frac{1}{2} \left(1 + \frac{\Delta^2}{EE'}\right) \left\{ [1 - f(E)][1 - f(E')]n(\Omega) - f(E)f(E')[n(\Omega) + 1] \right\}. \quad (6e)$$

Numerical solutions to Eq. (1a), (1b), (5a-e) were obtained with a forward Euler scheme, where the integrals were evaluated numerically with a trapezoidal method at each timestep. Where applicable, vectorized operations were used to speed up the computation. We introduced a cutoff above the maximum acoustic phonon energy for the integral bounds in Eqs. (1a) and (1b) while ensuring that the numerical solutions were not affected by the choice of a larger cutoff and remained below our error criteria. As discussed in Appendix VII C, Eqs. (11) and (12) are solved self-consistently for a given  $I_B$  to determine  $\rho(E)$  and  $|\Delta| = |\Delta(I_B, T)|$ . Details on obtaining the numerical solutions to the Usadel equation are discussed in Appendix VII C. At each time step, it was checked that the total energy of the electronic system

$$E_e = 4N(0)V_{\text{init}} \left\{ \int_{|\Delta|}^{\infty} dE E \rho(E) f(E) - \frac{|\Delta|^2}{4} \left( \frac{1}{2} + \ln \frac{\Delta_0}{|\Delta|} \right) \right\} \quad (7)$$

and the phonon system

$$E_{\text{vib}} = V_{\text{init}} \int_0^{\infty} d\Omega \Omega N F(\Omega) n(\Omega) \quad (8)$$

is conserved within 0.1% of the starting energy for  $t \leq \tau_{\Delta}$  when  $\tau_{\text{esc}} = \infty$ . In most of our simulations, this error criterion was often exceeded by orders of magnitude. It was also checked that increasing the number of discrete energies and time steps used in the numerical solutions did not change the calculation results significantly. We found using a grid of energies spaced by  $\sim \Delta/15$  and a grid of times spaced by 10 fs sufficient to meet our error criteria by approximately an order of magnitude in most cases. For the simulations of optical irradiation in NbN, with  $\tau_{\text{esc}} = 10$  ps, about  $\sim 25\%$  of the photon energy was lost to the substrate.

To determine the phonon-bubble initial condition for the SNSPD simulations, we use Eq. (1b) and approximate the initial excess quasiparticle distribution  $\delta f(E) = f(E) - f^{\text{eq}}(E)$  as a delta function centered at  $E_{\lambda}$ , which gives that the initial phonon population is  $n_0(\Omega) = \beta(E_{\lambda})\alpha^2(\Omega)$  [7], where the parameter  $\beta(E_{\lambda})$  ensures that the initial energy of the phonon system is equal to the photon energy. Thus,  $n_0(\Omega)$  and an equilibrium quasiparticle (Fermi-Dirac) distribution  $f^{\text{eq}}(E)$  characterize the phonon bubble. Eqs. (1a) and (1b) with the phonon-bubble initial condition then provide the subsequent quasiparticle and phonon dynamics that result from the absorption of a photon. In principle, one could instead use an initial condition with a delta function centered at  $E_{\lambda}$  for  $f(E)$  and an equilibrium distribution for  $n(\Omega)$ . However, a solution over the full range of energies up to  $E_{\lambda}$  is a computationally expensive task, and the initial phonon bubble allows us to significantly reduce the computational burden.

In Fig. 6a, we plot the time evolution of the excess quasiparticle  $\delta f(E)$  and phonon distributions  $\delta n(\Omega)$  resulting from the ‘‘phonon bubble’’ initial condition in NbN when considering the full-bandwidth electron-phonon coupling and phonon density of states as computed with DFPT calculations. The  $\delta f(E)$  and  $\delta n(\Omega)$  resulting from the Debye approximation are also plotted in Fig. 6b for comparison with the results obtained with the exact form of  $\alpha^2 F(\Omega)$  and  $F(\Omega)$ . The qualitative behavior between the solutions of the kinetic equations with the DFPT and Debye models is similar. However, the electron-phonon coupling leads to non-trivial changes in the generated quasiparticle and phonon populations. We also note that the discontinuity in the phonon distribution near  $\Omega = 2|\Delta|$  is more prominent with the Debye model. However, unlike in Ref. [7], the  $2|\Delta|$  discontinuity is smeared since we incorporate the effects of the finite  $\rho(E)$  resulting from a nonzero bias current. For NbN, it was found that the Debye model generally overestimates the rate of quasiparticle generation, which is reflected in Fig. 4b of the main text, where it can be seen that the prediction of  $I_{\text{det}}$  from the Debye model is consistently below the experimental data and predictions of the *ab initio* model.

For the transmon simulations, an initial volume of  $V_{\text{init}} = d^3$  was chosen as it is a natural length scale of the device that is consistent across every material. Since we are most interested in the energy density deposited into the superconductor, which can be computed from Geant4 simulations, this choice is appropriate to describe dynamics.

## B. Time-dependent Ginzburg-Landau equation

As discussed in the main text, we connect the results for the microscopic dynamics of the quasiparticle and phonon systems to the mesoscopic dynamics of  $\Delta$  via the time-dependent Ginzburg-Landau (TDGL) equation. This is useful in the case of modeling optical irradiation since phase-slip dynamics are naturally captured by the TDGL equation

$$\frac{u}{\sqrt{1 + \gamma^2 |\psi|^2}} \left( \frac{\partial}{\partial t} + i\mu + \frac{1}{2} \gamma^2 \frac{\partial |\psi|^2}{\partial t} \right) \psi = \xi^2 (\nabla - 2ie\mathbf{A})^2 \psi + (\alpha - |\psi|^2) \psi, \quad (9)$$

where we have used dimensionless units with  $u = \pi^4/14\zeta(3) = 5.79$ ,  $\gamma = 10$ , the normalized superconducting order parameter  $\psi = \Delta/|\Delta_0|$ , and the electric scalar potential  $\mu(\mathbf{r}, t)$  which satisfies a Poisson equation [66]. The parameter

$$\alpha(\mathbf{r}, t) = (1 - T/T_c - \varepsilon(\mathbf{r}, t))/(1 - T/T_c) \quad (10)$$

models the photon-induced suppression of  $\psi$  at position  $\mathbf{r}$  and time  $t$  ( $\alpha = 1$  at equilibrium), where  $\varepsilon(\mathbf{r}, t)$  is calculated from the microscopic dynamics using Eq. (3). Here,

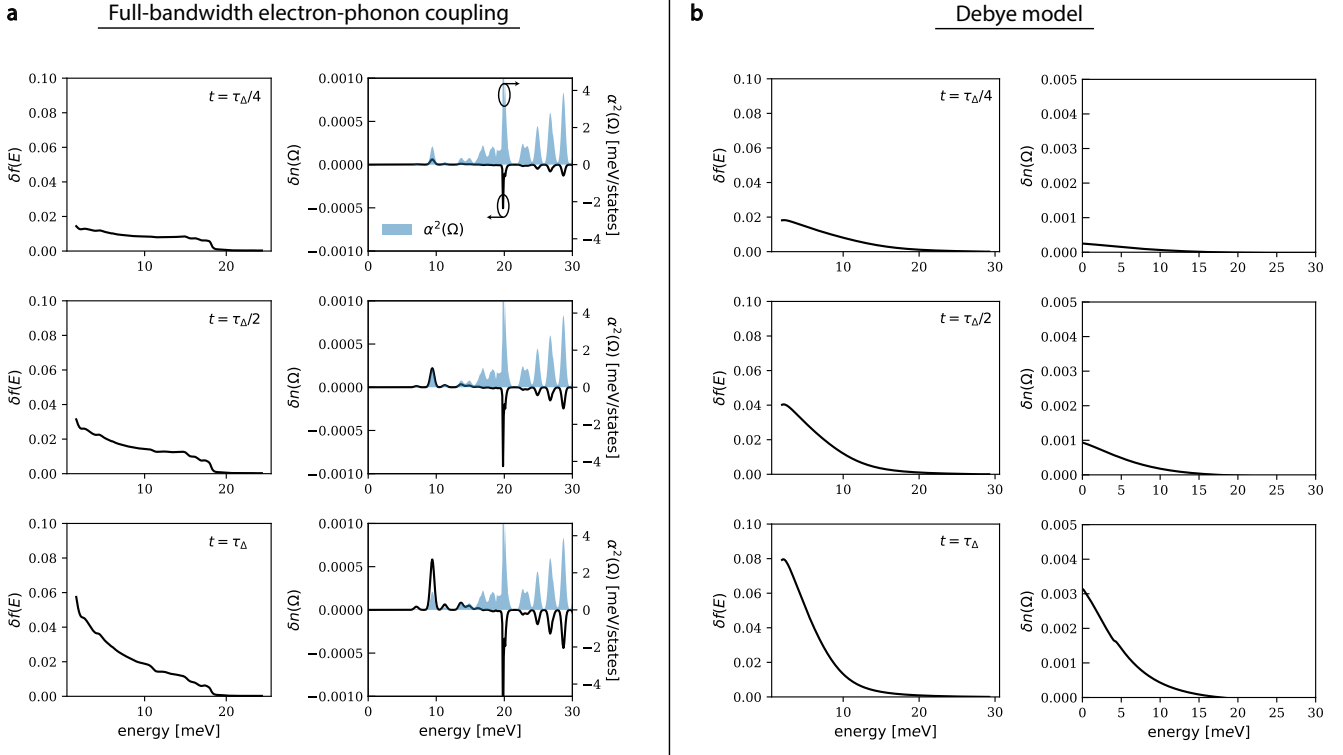


FIG. 6. Evolution of the excess quasiparticle  $\delta f(E)$  and phonon  $\delta n(\Omega)$  distributions for  $t = \tau_\Delta/4$ ,  $\tau_\Delta/2$ , and  $\tau_\Delta$ . (a) Calculations using the full-bandwidth electron-phonon coupling and phonon density of states as determined by DFPT calculations. In these figures,  $\alpha^2(\Omega)$  is plotted alongside  $\delta n(\Omega)$  to demonstrate the role of the electron-phonon coupling in determining the evolution of the phonon distribution. (b) The evolution of  $\delta f(E)$  and  $\delta n(\Omega)$  assuming a Debye approximation for the electron-phonon coupling and phonon density of states.

we assume that the hotspot grows isotropically with a time-dependent radius  $|\mathbf{r}(t)| = \sqrt{Dt}$ . A more rigorous treatment of quasiparticle and phonon diffusion, along with solving Eqs. (1a) and (1b) self-consistently with Eq. (2), would significantly improve the accuracy for wires with larger  $w$ , which possess longer latency times between absorption and detection. We also note that  $\tau_{\text{th}} > \tau_\Delta$  implies the local electron and phonon temperatures are still evolving when the region of suppressed superconductivity has diffused beyond  $V_{\text{init}}$ . Hence, caution must be exercised when assuming a well-defined electron and phonon temperature exists during the early stages of the quasiparticle cascade; however, a rigorous treatment of the microscopic diffusion could help address this issue. The generalized TDGL equation with Usadel corrections for the supercurrent density  $j_S$  and  $\Delta$  can also be used in place of Eq. (9) to improve validity at lower temperatures and large deviations from equilibrium [13]. Incorporating thermal equations for the electron and phonon temperatures and a circuit model to account for Joule heating, the kinetic inductance of the film, and the external circuitry will further improve the quantitative accuracy. These additional equations are most relevant in the presence of a small shunt resistance or small  $I_B$ , where these processes may play a role in the initial phase slip and in

initiating thermal runaway. This would likely improve the quantitative agreement at shorter  $\lambda_{\text{ph}}$  for  $w = 30$  nm and  $D = 0.5 \text{ cm}^2/\text{s}$  in Fig. 3d. However, as presented, the current model is sufficient to obtain reasonable quantitative accuracy.

We solve Eq. (9) with the Python package pyTDGL [67]. In these simulations, for each photon wavelength  $\lambda_{\text{ph}}$ , we varied  $I_B$  while checking if the voltage arising from the formation of a normal strip across the wire exceeded a threshold and the phase difference across the terminals of the device exceeded  $2\pi$ . The current at which these criteria were met was determined to be the detection current  $I_{\text{det}}$ . Note that since we perform the simulation over a coarse grid of bias currents, some quantization error is introduced. We restricted our simulation time to  $t < 15$  ps for the wires with  $w = 30$  nm and  $w = 50$  nm and  $t < 25$  ps for  $w = 85$  nm to account for the longer latency between photon absorption and detection. For the epitaxial detector, where diffusion was much faster, with  $w = 20$  nm the simulation time was restricted to  $t < 5$  ps. Material parameters were kept consistent between the microscopic and TDGL simulations. In the simulations for  $w = 20$  nm, 30 nm, and 50 nm, the max edge length of the two-dimensional mesh was set to  $2\xi_c$ . For  $w = 85$  nm, the max edge length was

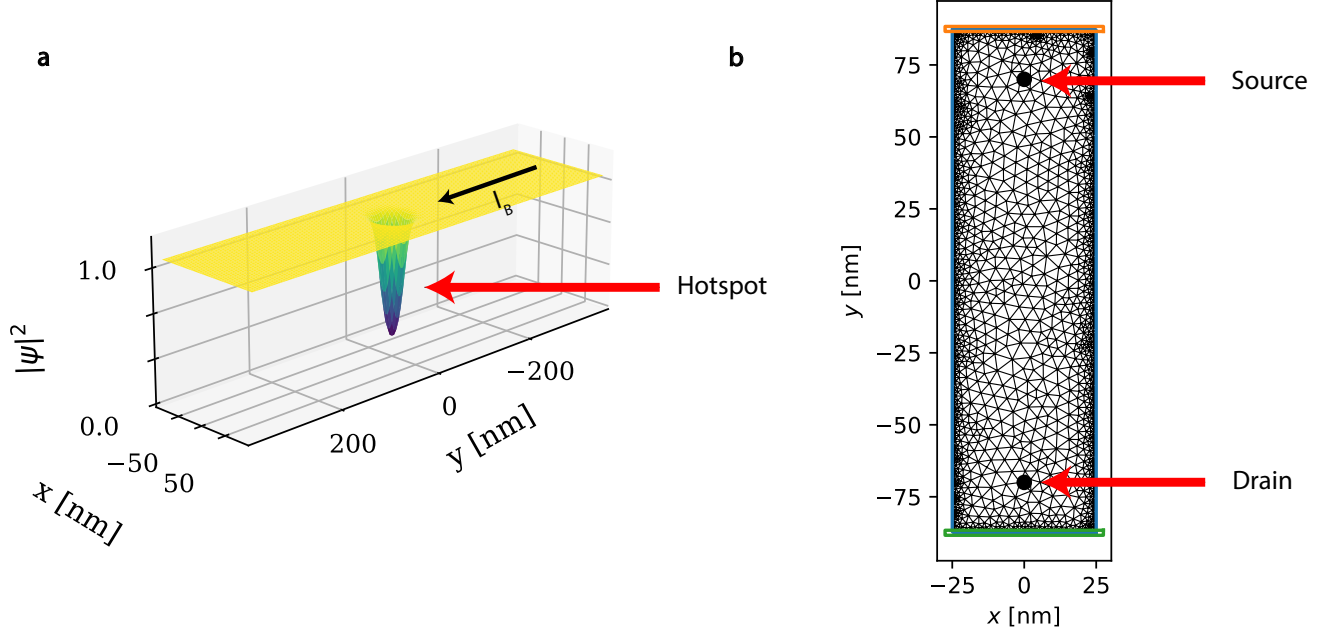


FIG. 7. Time-dependent Ginzburg-Landau simulation of the suppression of the normalized superconducting order parameter  $\psi$  following the absorption of a photon. (a) Magnitude of  $|\psi|^2$  after photon absorption. The photon-induced hotspot is labeled with a red arrow, and the direction of the bias current  $I_B$  from source to drain is indicated by the black arrow. (b) Meshing used in pyTDGL for numerical solutions of the TDGL equations for a wire width of  $w = 50$  nm. The source and drain for the current are labeled with red arrows.

set to  $2.5\xi_c$  to decrease runtime. Examples of the meshing are displayed in Fig. 7. By default, the pyTDGL package only allows for simulations down to  $T = T_c/2$ , so to simulate the behavior of the experimental data for SNSPDs in Ref. [49] and [50], where the SNSPDs were measured at  $T \approx 0.2T_c$ , we adjusted the zero temperature values of  $\xi_c$  and  $\lambda_L$  using their temperature dependencies from TDGL to make them consistent with the values at  $T = 0.2T_c$ .

### C. The Usadel equation

The normalized quasiparticle density of states for a superconducting film in the dirty limit is given by  $\rho(E) = \text{Re}\{\cos \Theta(E)\}$ , where  $\Theta(E)$  can be obtained from the Usadel equation on the imaginary-frequency axis

$$\begin{aligned} \hbar D \nabla^2 \Theta(\vec{r}, i\omega_n) + 2|\Delta(\vec{r})| \cos \Theta(\vec{r}, i\omega_n) \\ - \left( 2\hbar\omega_n + \frac{D}{\hbar} q^2 \cos \Theta(\vec{r}, i\omega_n) \right) \sin \Theta(\vec{r}, i\omega_n) = 0 \end{aligned} \quad (11)$$

and performing an analytical continuation to the real-frequency axis  $i\omega_n \rightarrow E + i0^+$ . For a uniform film, the spatial dependence of  $\Theta$  and  $|\Delta|$  can be ignored, there are no central boundary conditions, and the diffusive term  $\hbar D \nabla^2 \Theta(\vec{r}, i\omega_n)$  is zero. The order parameter  $|\Delta|$  satisfies

the BCS self-consistency equation

$$|\Delta| \ln \left( \frac{T}{T_c} \right) + 2\pi k_B T \sum_{\omega_n \geq 0} \left( \frac{|\Delta|}{\hbar\omega_n} - \sin \Theta(i\omega_n) \right) = 0, \quad (12)$$

where  $k_B$  is the Boltzmann constant,  $T_c$  is the critical temperature,  $\omega_n = \pi T(2n+1)k_B/\hbar$  is the  $n$ -th Matsubara frequency, and  $\Theta(i\omega_n)$  is the pairing-angle parametrization of the Nambu-Gor'kov Green's function [68, 69]. The full Migdal-Eliashberg self-consistency equations on the real-frequency axis, along with the strong-coupling Usadel equation [69], could be used instead of the BCS self-consistency equation (Eqs. (2) and (12)); however, the resulting complexity and effort to solve these equations would have been significant and beyond the scope of the current work. This approximation limits the quantitative accuracy of our model. The superfluid momentum  $q$  is related to the supercurrent density via

$$j_S = \frac{I_B}{wd} = \frac{2\pi k_B T}{|e|} \sigma_0 q \sum_{n=0}^{\infty} \sin^2 \Theta(i\omega_n), \quad (13)$$

where  $\sigma_0 = 1/\rho_N$  is the Drude conductivity. We define the spectral function

$$R(E, \Delta) = \text{Im}\{\sin \Theta(E)\} \quad (14)$$

from the main text.

Eqs. (11) and (12) are solved simultaneously with a left-preconditioned Newton-Krylov method [70, 71]. The

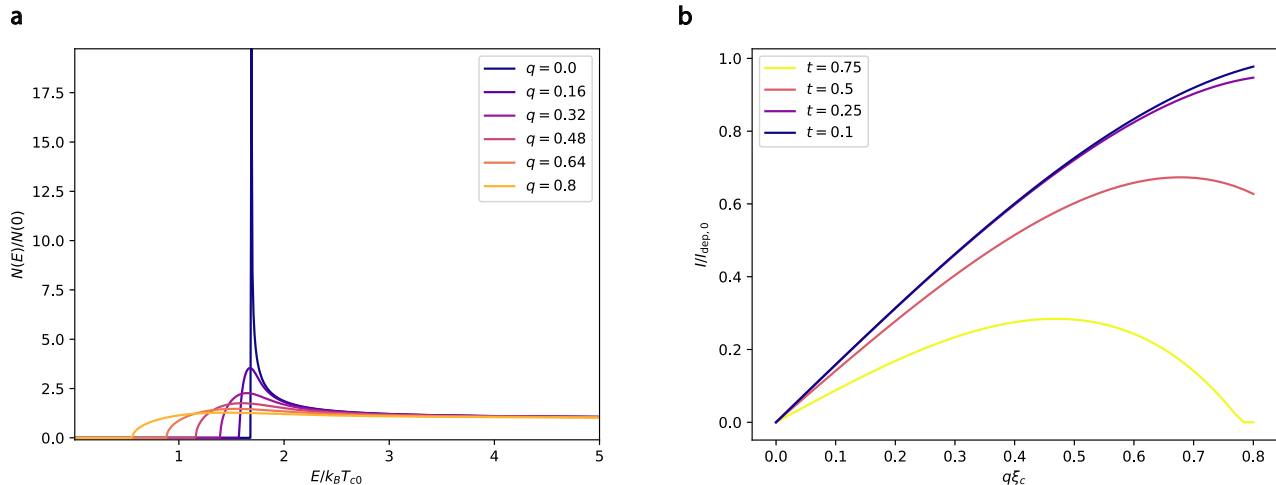


FIG. 8. (a) The normalized quasiparticle density of states  $\rho(E) = N(E)/N(0)$  for several values of the superfluid momentum  $q$  at  $T \sim 0$  K. (b) The supercurrent  $I = j/wd$  normalized to the depairing current at zero temperature  $I/I_{\text{dep},0}$  for several values of the reduced temperature  $t = T/T_c$ .

preconditioner is constructed by sparsifying the Jacobian of Eqs. (11) and (12) assuming a BCS ( $q = 0$ ) solution. The infinite Matsubara sum in Eq. (12) is approximated with a quadrature rule for sums [72].

A nonzero bias current induces a smearing of the singularity at the gap-edge  $\Delta$  in the quasiparticle density of states  $\rho(E)$ . As discussed above, for simplicity, we solve the Usadel equation in the weak-coupling limit, which differs from the strong-coupling form by a scaling factor in the self-consistency equation, an additional self-consistency equation for the wave-function renormalization parameter, and a frequency-dependent order parameter  $\Delta(i\omega_n)$ . In the strong-coupling case, these equations are more difficult to solve, but the relative shape of  $\rho(E)$  is qualitatively similar. To better match the experimental data for NbN, we scale the results of the weak-coupling theory by a factor of 2.1/1.76 to account for the strong-coupling nature of NbN and retain the expected relationship between  $\Delta$  and  $T_c$  ( $\Delta_0 = 2.1k_B T_c$ ) as predicted by Migdal-Eliashberg theory and observed experimentally [35]. For bias currents on the order of the depairing current, the smearing takes on a similar form as seen in Fig. 8a for different values of the superfluid momentum  $q$ . The superfluid momentum  $q$  is connected to the supercurrent via Eq. (13), and its solutions are shown in Fig. 8b for several different reduced temperatures  $t = T/T_c$ . The value of  $I$  at which  $dI/dq = 0$  is the temperature-dependent depairing current  $I_{\text{dep}}$ . In our solutions, we found that for  $0.5I_{\text{dep}} \leq I_B \leq 0.9I_{\text{dep}}$ , where  $I_{\text{dep}}$  is the depairing current, there was not a strong dependence of the generated quasiparticle population on  $I_B$ . Hence, we set  $I_B = 0.5I_{\text{dep}}$ , which incorporates the effect of smearing in  $\rho(E)$  while also preserving the generality of the results to polycrystalline devices with switching currents on the order of  $0.5I_{\text{dep}}$ .

#### D. Density functional theory calculations

We employed the Quantum Espresso code [73] to compute the structural, electronic, and harmonic phonon properties of the bulk materials using first-principles DFPT. The exchange-correlation functional was described by the Perdew-Burke-Ernzerhof (PBE) [74] version of the generalized gradient approximation (GGA) in combination with optimized norm-conserving Vanderbilt pseudopotentials [75, 76]. The convergence threshold for the self-consistent field was set to  $10^{-10}$  Ry for the energy difference between consecutive electronic steps and structural relaxations were performed until the forces on each atom were less than  $10^{-6}$  Ry/Å. A plane-wave kinetic energy cutoff of 80 Ry was used for all materials except Ta, where 140 Ry was used, along with an  $18 \times 18 \times 18$  k-point grid and a Methfessel-Paxton (MP) smearing [77] of 0.02 Ry to sample the Brillouin zone for self-consistent calculations. For NbN, the MP smearing had to be set to 0.2 Ry to avoid imaginary frequencies in the harmonic DFPT calculation of phonon properties, as disorder, impurities, and anharmonic effects are not accounted for. As can be appreciated in Fig. 2, the calculated phonon dispersion compares well to experimental data [19]. Spin-orbit coupling effects were included for Pb and Ta.

For phonon calculations, we employed a  $6 \times 6 \times 6$  q-point grid ( $8 \times 8 \times 8$  for Ta) and a threshold of self-consistency of  $10^{-14}$  Ry to obtain the dynamical matrices within the harmonic approximation. To improve convergence for NbN and Pb, we interpolated the electronic and phononic properties onto finer grids utilizing the Electron-Phonon Wannier (EPW) code [12]. Specifically, interpolation to fine grids of  $30 \times 30 \times 30$  for both electrons and phonons was performed to obtain isotropic Eliashberg spectral functions  $\alpha^2 F(\Omega)$ .

### E. Material Parameters

Symbol	NbN	Al	Nb	TiN	Pb	Ta
$N$ [nm <sup>3</sup> ]	48	60	55	37	33	56
$\rho_N$ [ $\Omega \cdot \text{nm}$ ]	1040	28	152	220	220	136
$E_F$ [eV]	5.895	11.7	5.32	4.2	10.87	5.32
$d$ [nm]	5	200	200	200	200	200
$\tau_{\text{esc}}$ [ps]	15	100	100	100	100	100
$\Delta$ [meV]	1.8	0.2	1.2	1.4	1.1	0.7
$T_c$ [K]	10	1.3	8	9	7	4.2

TABLE I. Material parameters used in the simulations in the main text for NbN, Al, Nb, TiN, Pb, and Ta.  $N$  is the ion density,  $\rho_N$  is the bulk resistivity,  $E_F$  is the Fermi energy,  $d$  is the device thickness for a superconducting nanowire single-photon detector for NbN and the thickness for a transmon qubit for Al, Nb, TiN, Pb, and Ta,  $\tau_{\text{esc}}$  is the corresponding characteristic time for phonon escape to the substrate,  $\Delta = |\Delta|$  is the magnitude of the superconducting order parameter, and  $T_c$  is the critical temperature. For the Cooper pair density  $n_{\text{cp}}$ , the quoted value in the literature of  $0.004 \text{ nm}^3$  was used for Al [61], and the rest were estimated using the London penetration depth.

Table I shows the material parameters used in the simulations of the main text. These values are approximate and can also be obtained *ab initio* from DFT rather than experimental data [3, 78]. For NbN,  $|\Delta|$  and  $T_c$  were set to resemble the expected values for a disordered polycrystalline film. The superconducting properties of all other materials were calculated from the BCS self-consistency equation and the DFPT calculations.

- 
- [1] G. Eliashberg, Interactions between electrons and lattice vibrations in a superconductor, *Sov. Phys. JETP* **11**, 696 (1960).
- [2] P. B. Allen and R. C. Dynes, Transition temperature of strong-coupled superconductors reanalyzed, *Phys. Rev. B* **12**, 905 (1975).
- [3] C. Pellegrini and A. Sanna, *Ab initio* methods for superconductivity, *Nature Reviews Physics* **6**, 509 (2024).
- [4] R. E. Prange, Transport Theory for Electron-Phonon Interactions in Metals, *Physical Review* **134**, A566 (1964).
- [5] G. M. Eliashberg, Film superconductivity stimulated by a high-frequency field, *JETP Lett. (USSR) (Engl. Transl.)*; (United States) **11** (1970).
- [6] G. Eliashberg, Inelastic electron collisions and nonequilibrium stationary states in superconductors, *Sov Phys JETP* **34**, 668 (1972).
- [7] J.-J. Chang and D. J. Scalapino, Kinetic-equation approach to nonequilibrium superconductivity, *Physical Review B* **15**, 2651 (1977).
- [8] P. Debye, Zur theorie der spezifischen wärmen, *Annalen der Physik* **344**, 789 (1912).
- [9] J. V. Ashby and G. Rickayzen, Detailed solutions for non-equilibrium superconductivity. I. Temperature-dependent solutions, *Journal of Physics F: Metal Physics* **11**, 2595 (1981).
- [10] D. Goldie and S. Withington, Non-equilibrium superconductivity in quantum-sensing superconducting resonators, *Superconductor Science and Technology* **26**, 015004 (2012).
- [11] R. Lucrezi, P. P. Ferreira, S. Hajinazar, H. Mori, H. Paudyal, E. R. Margine, and C. Heil, Full-bandwidth anisotropic migdal-eliasberg theory and its application to superhydrides, *Communications Physics* **7**, 33 (2024).
- [12] H. Lee, S. Poncé, K. Bushick, S. Hajinazar, J. Lafuente-Bartolome, J. Leveillee, C. Lian, J.-M. Lihm, F. Macheda, H. Mori, *et al.*, Electron-phonon physics from first principles using the epw code, *npj Computational Materials* **9**, 156 (2023).
- [13] D. Vodolazov, Single-Photon Detection by a Dirty Current-Carrying Superconducting Strip Based on the Kinetic-Equation Approach, *Physical Review Applied* **7**, 10.1103/PhysRevApplied.7.034014 (2017).
- [14] J. P. Allmaras, *Modeling and development of superconducting nanowire single-photon detectors* (California Institute of Technology, 2020).
- [15] R. Budoyo, J. B. Hertzberg, C. Ballard, K. Voigt, Z. Kim, J. Anderson, C. Lobb, and F. Wellstood, Effects of nonequilibrium quasiparticles in a thin-film superconducting microwave resonator under optical illumination, *Physical Review B* **93**, 024514 (2016).
- [16] C. H. Liu, D. C. Harrison, S. Patel, C. D. Wilen, O. Raftery, A. Shearow, A. Ballard, V. Iaia, J. Ku, B. L. T. Plourde, and R. McDermott, Quasiparticle poisoning of superconducting qubits from resonant absorption of pair-breaking photons, *Phys. Rev. Lett.* **132**, 017001 (2024).
- [17] R. Benevides, M. Drimmer, G. Bisson, F. Adinolfi, U. v. Lüpke, H. M. Doleman, G. Catelani, and Y. Chu, Quasiparticle dynamics in a superconducting qubit irradiated by a localized infrared source, *Phys. Rev. Lett.* **133**, 060602 (2024).
- [18] P. Ferreira, R. Lucrezi, I. Guilhon, M. Marques, L. Teles, C. Heil, and L. Eleno, *Ab initio* modeling of superconducting alloys, *Materials Today Physics* **48**, 101547 (2024).

- [19] A. Christensen, O. Dietrich, W. Kress, W. Teuchert, and R. Currat, Phonon anomalies in transition metal nitrides:  $\delta$ -nbn, *Solid State Communications* **31**, 795 (1979).
- [20] F. Marsili, V. B. Verma, J. A. Stern, S. Harrington, A. E. Lita, T. Gerrits, I. Vayshenker, B. Baek, M. D. Shaw, R. P. Mirin, and S. W. Nam, Detecting single infrared photons with 93% system efficiency, *Nature Photonics* **7**, 210 (2013), publisher: Nature Publishing Group.
- [21] D. V. Reddy, R. R. Nerem, S. W. Nam, R. P. Mirin, and V. B. Verma, Superconducting nanowire single-photon detectors with 98% system detection efficiency at 1550 nm, *Optica* **7**, 1649 (2020), publisher: Optica Publishing Group.
- [22] J. Chang, J. W. N. Los, J. O. Tenorio-Pearl, N. Noordzij, R. Gourgues, A. Guardiani, J. R. Zichi, S. F. Pereira, H. P. Urbach, V. Zwiller, S. N. Dorenbos, and I. Esmaeil Zadeh, Detecting telecom single photons with 99.5-2.07+0.5% system detection efficiency and high time resolution, *APL Photonics* **6**, 036114 (2021).
- [23] V. B. Verma, B. Korzh, A. B. Walter, A. E. Lita, R. M. Briggs, M. Colangelo, Y. Zhai, E. E. Wollman, A. D. Beyer, J. P. Allmaras, H. Vora, D. Zhu, E. Schmidt, A. G. Kozorezov, K. K. Berggren, R. P. Mirin, S. W. Nam, and M. D. Shaw, Single-photon detection in the mid-infrared up to 10  $\mu$ m wavelength using tungsten silicide superconducting nanowire detectors, *APL Photonics* **6**, 056101 (2021).
- [24] G. G. Taylor, A. B. Walter, B. Korzh, B. Bumble, S. R. Patel, J. P. Allmaras, A. D. Beyer, R. O'Brien, M. D. Shaw, and E. E. Wollman, Low-noise single-photon counting superconducting nanowire detectors at infrared wavelengths up to 29  $\mu$ m, *Optica* **10**, 1672 (2023).
- [25] Y. Hochberg, I. Charaev, S.-W. Nam, V. Verma, M. Colangelo, and K. K. Berggren, Detecting sub-gev dark matter with superconducting nanowires, *Phys. Rev. Lett.* **123**, 151802 (2019).
- [26] Y. Hochberg, New constraints on dark matter from superconducting nanowires, *Physical Review D* **106**, 10.1103/PhysRevD.106.112005 (2022).
- [27] B. Korzh, Q.-Y. Zhao, J. P. Allmaras, S. Frasca, T. M. Autry, E. A. Bersin, A. D. Beyer, R. M. Briggs, B. Bumble, M. Colangelo, G. M. Crouch, A. E. Dane, T. Gerrits, A. E. Lita, F. Marsili, G. Moody, C. Peña, E. Ramirez, J. D. Rezac, N. Sinclair, M. J. Stevens, A. E. Velasco, V. B. Verma, E. E. Wollman, S. Xie, D. Zhu, P. D. Hale, M. Spiropulu, K. L. Silverman, R. P. Mirin, S. W. Nam, A. G. Kozorezov, M. D. Shaw, and K. K. Berggren, Demonstration of sub-3 ps temporal resolution with a superconducting nanowire single-photon detector, *Nature Photonics* **14**, 250 (2020), publisher: Nature Publishing Group.
- [28] I. Charaev, E. K. Batson, S. Cherednichenko, K. Reidy, V. Drakinskiy, Y. Yu, S. Lara-Avila, J. D. Thomsen, M. Colangelo, F. Incalza, K. Ilin, A. Schilling, and K. K. Berggren, Single-photon detection using large-scale high-temperature MgB2 sensors at 20 K, *Nature Communications* **15**, 3973 (2024), publisher: Nature Publishing Group.
- [29] H. Shibata, H. Takesue, T. Honjo, T. Akazaki, and Y. Tokura, Single-photon detection using magnesium diboride superconducting nanowires, *Applied Physics Letters* **97**, 212504 (2010).
- [30] S. Cherednichenko, N. Acharya, E. Novoselov, and V. Drakinskiy, Low kinetic inductance superconducting MgB2 nanowires with a 130 ps relaxation time for single-photon detection applications, *Superconductor Science and Technology* **34**, 044001 (2021), publisher: IOP Publishing.
- [31] R. Arpaia, M. Ejrnaes, L. Parlato, F. Tafuri, R. Cristiano, D. Golubev, R. Sobolewski, T. Bauch, F. Lombardi, and G. P. Pepe, High-temperature superconducting nanowires for photon detection, *Physica C: Superconductivity and its Applications* **509**, 16 (2015).
- [32] R. Arpaia, Transport properties of ultrathin YBCO nanowires: A route to single-photon detection, *Physical Review B* **96**, 10.1103/PhysRevB.96.064525 (2017).
- [33] M. Ejrnaes, L. Parlato, R. Arpaia, T. Bauch, F. Lombardi, R. Cristiano, F. Tafuri, and G. P. Pepe, Observation of dark pulses in 10 nm thick YBCO nanostrips presenting hysteretic current voltage characteristics, *Superconductor Science and Technology* **30**, 12LT02 (2017), publisher: IOP Publishing.
- [34] I. Charaev, D. A. Bandurin, A. T. Bollinger, I. Y. Phinney, I. Drozdov, M. Colangelo, B. A. Butters, T. Taniguchi, K. Watanabe, X. He, O. Medeiros, I. Božović, P. Jarillo-Herrero, and K. K. Berggren, Single-photon detection using high-temperature superconductors, *Nature Nanotechnology* **18**, 343 (2023), publisher: Nature Publishing Group.
- [35] A. D. Semenov, G. N. Gol'tsman, and A. A. Korneev, Quantum detection by current carrying superconducting film, *Physica C: Superconductivity* **351**, 349 (2001).
- [36] A. D. Semenov, R. S. Nebosis, Y. P. Gousev, M. A. Heusinger, and K. F. Renk, Analysis of the nonequilibrium photoresponse of superconducting films to pulsed radiation by use of a two-temperature model, *Phys. Rev. B* **52**, 581 (1995).
- [37] A. J. Kerman, J. K. W. Yang, R. J. Molnar, E. A. Dauler, and K. K. Berggren, Electrothermal feedback in superconducting nanowire single-photon detectors, *Phys. Rev. B* **79**, 100509 (2009).
- [38] J. K. W. Yang, A. J. Kerman, E. A. Dauler, V. Anant, K. M. Rosfjord, and K. K. Berggren, Modeling the electrical and thermal response of superconducting nanowire single-photon detectors, *IEEE Transactions on Applied Superconductivity* **17**, 581 (2007).
- [39] J. R. Clem and K. K. Berggren, Geometry-dependent critical currents in superconducting nanocircuits, *Phys. Rev. B* **84**, 174510 (2011).
- [40] A. G. Kozorezov, J. K. Wigmore, D. Martin, P. Verhoeve, and A. Peacock, Electron energy down-conversion in thin superconducting films, *Phys. Rev. B* **75**, 094513 (2007).
- [41] A. G. Kozorezov, A. F. Volkov, J. K. Wigmore, A. Peacock, A. Poelaert, and R. den Hartog, Quasiparticle-phonon downconversion in nonequilibrium superconductors, *Phys. Rev. B* **61**, 11807 (2000).
- [42] D. Y. Vodolazov, Current dependence of the red boundary of superconducting single-photon detectors in the modified hot-spot model, *Physical Review B* **90**, 054515 (2014).
- [43] A. Engel, J. J. Renema, K. Il'in, and A. Semenov, Detection mechanism of superconducting nanowire single-photon detectors, *Superconductor Science and Technology* **28**, 114003 (2015).
- [44] K. K. Berggren, Q.-Y. Zhao, N. Abebe, M. Chen, P. Ravindran, A. McCaughan, and J. C. Bardin, A superconducting nanowire can be modeled by using spice, *Superconductor Science and Technology* **31**, 055010 (2018).

- [45] A. D. Semenov, Superconducting nanostrip single-photon detectors some fundamental aspects in detection mechanism, technology and performance, *Superconductor Science and Technology* **34**, 054002 (2021).
- [46] S. B. Kaplan, C. Chi, D. Langenberg, J.-J. Chang, S. Jafarey, and D. Scalapino, Quasiparticle and phonon lifetimes in superconductors, *Physical Review B* **14**, 4854 (1976).
- [47] K. S. Il'in, I. I. Milostnaya, A. A. Verevkin, G. N. Gol'tsman, E. M. Gershenzon, and R. Sobolewski, Ultimate quantum efficiency of a superconducting hot-electron photodetector, *Applied Physics Letters* **73**, 3938 (1998), <https://pubs.aip.org/aip/apl/article-pdf/73/26/3938/18538627/3938.1.online.pdf>.
- [48] S. P. Chockalingam, M. Chand, J. Jesudasan, V. Tripathi, and P. Raychaudhuri, Superconducting properties and hall effect of epitaxial nbn thin films, *Phys. Rev. B* **77**, 214503 (2008).
- [49] R. Cheng, J. Wright, H. G. Xing, D. Jena, and H. X. Tang, Epitaxial niobium nitride superconducting nanowire single-photon detectors, *Applied Physics Letters* **117**, 132601 (2020), <https://pubs.aip.org/aip/apl/article-pdf/doi/10.1063/5.0018818/14539879/132601.1.online.pdf>.
- [50] F. Marsili, F. Bellei, F. Najafi, A. E. Dane, E. A. Dauler, R. J. Molnar, and K. K. Berggren, Efficient single photon detection from 500 nm to 5  $\mu$ m wavelength, *Nano letters* **12**, 4799 (2012).
- [51] R. Gourgues, J. W. N. Los, J. Zichi, J. Chang, N. Kalhor, G. Bulgarini, S. N. Dorenbos, V. Zwiller, and I. E. Zadeh, Superconducting nanowire single photon detectors operating at temperature from 4 to 7 k, *Opt. Express* **27**, 24601 (2019).
- [52] L. N. Bulaevskii, M. J. Graf, and V. G. Kogan, Vortex-assisted photon counts and their magnetic field dependence in single-photon superconducting detectors, *Phys. Rev. B* **85**, 014505 (2012).
- [53] A. G. Kozorezov, C. Lambert, F. Marsili, M. J. Stevens, V. B. Verma, J. P. Allmaras, M. D. Shaw, R. P. Mirin, and S. W. Nam, Fano fluctuations in superconducting-nanowire single-photon detectors, *Phys. Rev. B* **96**, 054507 (2017).
- [54] D. Salvoni, M. Ejrnaes, A. Gaggero, F. Mattioli, F. Martini, H. Ahmad, L. Di Palma, R. Satariano, X. Yang, L. You, F. Tafuri, G. Pepe, D. Massarotti, D. Montemurro, and L. Parlato, Activation energies in MoSi/Al superconducting nanowire single-photon detectors, *Phys. Rev. Appl.* **18**, 014006 (2022).
- [55] H. Bartolf, A. Engel, A. Schilling, K. Il'in, M. Siegel, H.-W. Hübers, and A. Semenov, Current-assisted thermally activated flux liberation in ultrathin nanopatterned nbn superconducting meander structures, *Phys. Rev. B* **81**, 024502 (2010).
- [56] P. Li, P. M. Wu, Y. Bomze, I. V. Borzenets, G. Finkelstein, and A. M. Chang, Switching currents limited by single phase slips in one-dimensional superconducting al nanowires, *Phys. Rev. Lett.* **107**, 137004 (2011).
- [57] K. A. Sunter and K. K. Berggren, Optical modeling of superconducting nanowire single photon detectors using the transfer matrix method, *Appl. Opt.* **57**, 4872 (2018).
- [58] M. Csete, Á. Sipos, A. Szalai, F. Najafi, G. Szabó, and K. K. Berggren, Improvement of infrared single-photon detectors absorptance by integrated plasmonic structures, *Scientific Reports* **3**, 2406 (2013).
- [59] V. Anant, A. J. Kerman, E. A. Dauler, J. K. W. Yang, K. M. Rosfjord, and K. K. Berggren, Optical properties of superconducting nanowire single-photon detectors, *Opt. Express* **16**, 10750 (2008).
- [60] R. Acharya, L. Aghababaie-Beni, I. Aleiner, T. I. Andersen, M. Ansmann, F. Arute, K. Arya, A. Asfaw, N. Astrakhantsev, J. Atalaya, *et al.*, Quantum error correction below the surface code threshold, *arXiv preprint arXiv:2408.13687* (2024).
- [61] A. P. Vepsäläinen, A. H. Karamlou, J. L. Orrell, A. S. Dogra, B. Loer, F. Vasconcelos, D. K. Kim, A. J. Melville, B. M. Niedzielski, J. L. Yoder, *et al.*, Impact of ionizing radiation on superconducting qubit coherence, *Nature* **584**, 551 (2020).
- [62] K. Serniak, M. Hays, G. de Lange, S. Diamond, S. Shankar, L. D. Burkhardt, L. Frunzio, M. Houzet, and M. H. Devoret, Hot nonequilibrium quasiparticles in transmon qubits, *Phys. Rev. Lett.* **121**, 157701 (2018).
- [63] R. Linehan, I. Hernandez, D. Temples, S. Dang, D. Baxter, L. Hsu, E. Figueroa-Feliciano, R. Khatiwada, K. Anyang, D. Bowering, *et al.*, Estimating the energy threshold of phonon-mediated superconducting qubit detectors operated in an energy-relaxation sensing scheme, *Physical Review D* **111**, 063047 (2025).
- [64] D. M. Tennant, L. A. Martinez, K. M. Beck, S. R. O'Kelley, C. D. Wilen, R. McDermott, J. L. DuBois, and Y. J. Rosen, Low-frequency correlated charge-noise measurements across multiple energy transitions in a tantalum transmon, *PRX Quantum* **3**, 030307 (2022).
- [65] A. P. Place, L. V. Rodgers, P. Mundada, B. M. Smitham, M. Fitzpatrick, Z. Leng, A. Premkumar, J. Bryon, A. Vrajitoarea, S. Sussman, *et al.*, New material platform for superconducting transmon qubits with coherence times exceeding 0.3 milliseconds, *Nature communications* **12**, 1779 (2021).
- [66] L. Kramer and R. J. Watts-Tobin, Theory of dissipative current-carrying states in superconducting filaments, *Phys. Rev. Lett.* **40**, 1041 (1978).
- [67] L. Bishop-Van Horn, pyTDGL: Time-dependent Ginzburg-Landau in python, *Comput. Phys. Commun.* **291**, 108799 (2023).
- [68] K. D. Usadel, Generalized diffusion equation for superconducting alloys, *Physical Review Letters* **25**, 507 (1970).
- [69] J. Rammer, Strong-coupling calculation of the lower critical field in high- $T_c$  superconductors, *Phys. Rev. B* **36**, 5665 (1987).
- [70] D. A. Knoll and D. E. Keyes, Jacobian-free newton-krylov methods: a survey of approaches and applications, *Journal of Computational Physics* **193**, 357 (2004).
- [71] P. Virtanen, Magnetoelectric effects in diffusive two-dimensional superconductors studied by the nonlinear  $\sigma$  model, *Physical Review B* **111**, 024510 (2025).
- [72] H. Monien, Gaussian summation, *Explicit Methods in Number Theory* **12**, 1809 (2016).
- [73] P. Giannozzi, O. Andreussi, T. Brumme, O. Bunau, M. B. Nardelli, M. Calandra, R. Car, C. Cavazzoni, D. Ceresoli, M. Cococcioni, *et al.*, Advanced capabilities for materials modelling with quantum espresso, *Journal of physics: Condensed matter* **29**, 465901 (2017).
- [74] J. P. Perdew, K. Burke, and M. Ernzerhof, Generalized gradient approximation made simple, *Physical review letters* **77**, 3865 (1996).

- [75] M. Schlipf and F. Gygi, Optimization algorithm for the generation of oncv pseudopotentials, *Computer Physics Communications* **196**, 36 (2015).
- [76] D. Hamann, Optimized norm-conserving vanderbilt pseudopotentials, *Physical Review B—Condensed Matter and Materials Physics* **88**, 085117 (2013).
- [77] M. Methfessel and A. Paxton, High-precision sampling for brillouin-zone integration in metals, *physical review B* **40**, 3616 (1989).
- [78] F. Giustino, *Materials modelling using density functional theory: properties and predictions* (Oxford University Press, 2014).